Research Article | Vol. 30, No. 9 / 25 Apr 2022 / Optics Express 14002
Optics EXPRESS

Realization of ultrawide-angle high transmission and its applications in 5G millimeter-wave communications

ZHE ZHANG,[1] ZHIYUAN CHE,[1] JINGGUANG CHEN,[1] JIANPING ZENG,[1] HAO HUANG,[1] FANG GUAN,[1,2,3,5] LEI SHI,[1,4,6] XIAOHAN LIU,[1] AND JIAN ZI[1,4]

[1]*State Key Laboratory of Surface Physics, Key Laboratory of Micro- and Nano-Photonic Structures (Ministry of Education) and Department of Physics, Fudan University, Shanghai 200438, China*
[2]*Peng Cheng Laboratory, Shenzhen 518000, China*
[3]*Zhangjiang Fudan International Innovation Center, Fudan University, Shanghai 201210, China*
[4]*Collaborative Innovation Center of Advanced Microstructures, Nanjing University, Nanjing 210093, China*
[5]*fguan@fudan.edu.cn*
[6]*lshi@fudan.edu.cn*

Abstract: By using single-layer metasurfaces, we realized ultrawide-angle high-transmission in the millimeter-wave band, which allowed more than 98% transmission of dual-polarized electromagnetic waves for almost all incident angles. The multipolar expansion method was used to analyze and verify the condition of the generalized Kerker effect at the corresponding reflected angles. Using quartz glass substrates with the same metallic periodic structures, electromagnetic windows are proposed that can improve any-directed 5G millimeter-wave communication signals from outdoor to indoor environments. The proposed interpretations can connect the Kerker effect with actual applications and enable the design of easy-to-integrate all-angle Kerker effect metasurface devices.

1. Introduction

Transmission is a fundamental property of electromagnetic (EM) waves [1,2]. In many systems, it is desirable to achieve an arbitrarily tailored transmission property. Wide-angle high-transmission (WAHT) characteristics are extremely important in many application scenarios, such as radomes [3,4], 5G millimeter-wave (mmWave) communications [5], invisibility cloaks [6–9], and optical devices [10–12]. For natural dielectric materials, the dual-polarized WAHT property has rarely been implemented owing to the general impedance mismatch [13]. In the past decades, owing to the rich electric and magnetic responses beyond those of natural materials, artificial metamaterials have been proposed and applied to almost the entire electromagnetic spectrum, which can realize more unusual electromagnetic properties [14–25]. Recently, as a type of ultrathin metamaterial, metasurfaces have attracted much attentions from engineers and scientists [26–42]. WAHT has been studied by many researchers using these artificial structures, such as, complex multi-layers 2D or 3D metasurfaces [43–48], photonic crystal [49–51], etc. But, in practice, it is still very difficult to realize WAHT or even ultra-WAHT (UWAHT) by simple single-layer metasurface, especially those that need to be used in real engineering applications.

To analyze this problem better, based on Huygens–Fresnel principle, the unit cells in metasurface can be considered as many point sources when EM plane wave impinges from any incident directions. Reflection and transmission can be regarded as the re-radiation of these point sources. This inspires us that the radiation of single unit cell can be adjusted to modulate transmission properties. Fortunately, in 1983, Kerker, Wang, and Giles proved that the backscattering with a magnetic sphere can be totally eliminated when it satisfies the condition $\varepsilon = \mu$ [52], which is

#454720 https://doi.org/10.1364/OE.454720
Journal © 2022 Received 26 Jan 2022; revised 13 Mar 2022; accepted 24 Mar 2022; published 11 Apr 2022

Optics EXPRESS

called as Kerker effect. This phenomenon is caused by destructive interference of electric and magnetic dipolar components in excited magnetic sphere. Recently, the simple high refractive index (HRI) dielectric structures have attracted more attentions due to the abundant multipolar responses, which can be designed as different shapes and sizes to control forward or backward scattering greatly. Based on the principle of Kerker effect, in Ref. [53] and [54], the generalized Brewster effect (GBE) of HRI nanostructure metasurface was realized. It was really helpful that near-full-transmission of EM waves on the metasurface can be expressed by a zero-point on the electric radiated far-field pattern in the reflected direction, which achieves the Kerker condition of both electric and magnetic dipoles in the same unit cell. Furthermore, the extended Kerker effect has been discussed, which can realize in any other scattering angles by any-ordered multipoles, that is so-called generalized Kerker effect (GKE) [55]. Through the realization of Kerker effect at specific reflected direction, a simple and general model has been described to realize random dual-polarized GBE on ordinary dielectric interface [56]. The importance is that this model can allow us to consider the multipolar properties of dielectric firstly, and then add the appropriate designed metasurface structure to achieve Kerker effect. Evidently, GBE can only express near-full-transmission of EM plane waves at single incident angle. However, UWAHT phenomenon involves almost all incident angles of the EM plane wave for metasurfaces. Fortunately, the previous works inspire us that the similar multipolar analysis can be performed to design Kerker effect at any reflected directions, which can be called as all-angle Kerker effect (KE).

In this study, we designed two metasurfaces to realize UWAHT. First, the transmission properties and multipolar components of single-layer dielectric substrate are discussed. Based on these, the separate modulation method of dual-polarized EM plane wave and S-ring metasurface structure are proposed. Second, a dual-polarized S-ring metasurface was designed in the mmWave band. The transmittance is approximately 98% up to an incident angle θ_{in} close to 89.5° for s- or p-polarization at $f = 28.36$ GHz. The multipolar expansion method was used to analyze the multipolar components in one unit cell, and obvious dips can be found in the reflected directions, which can verify the correctness of the proposed principle. Third, a near-isotropic metasurface that can be used to improve the transmitted intensity of 5G mmWave signals from base stations to indoor terminals is proposed, which can be called an electromagnetic window (EMW). For this metasurface, the transmittance of the s-polarized EM wave is approximately 97% up to grazing incidence and transmittance of the p-polarized EM is larger than 90% up to incident angle $\theta_{\text{in}} = 80°$ at $f = 27.83$ GHz. Finally, two samples, designated I and II, were fabricated on a PCB dielectric substrate and quartz glass, respectively. The transmission coefficients were tested using a microwave measurement system. For sample I, the s-polarized transmittance $T_s \geq 80\%$ at frequency $f = 28.25 - 28.5$ GHz up to incident angle $\theta_{\text{in}} = 80°$. The p-polarized transmittance $T_p \geq 80\%$ at frequency $f = 26 - 29.5$ GHz when the incident angle was $\theta_{\text{in}} \leq 80°$. For sample II, at incident planes $\varphi = 0°$ and $\varphi = 45°$, the T_s exceeds 80% at frequency $f = 27.4 - 28.3$ GHz up to incident angle $\theta_{\text{in}} = 80°$, and T_p exceeds 80% at the entire experimental frequency domain $f = 26 - 29$ GHz when the incident angle $\theta_{\text{in}} \leq 80°$.

2. Realization methods and selection of the unit cell

As we all know, in the microwave band, the metallic metasurface or other planar array structures are fabricated on the dielectric substrate by printed circuit board (PCB) process. Through the discussions in the Section 1, when UWAHT is considered to realize, the influences of substrate and metallic structures on transmission can be studied respectively. As shown in Fig. 1, the transmission property of a ideal dielectric substrate can be calculated by full-wave simulation software in the millimeter-wave band. In Fig. 1 (a) and (c), we can clearly find that s-polarized transmittance T_s is really low when incident angle θ_{in} gets larger in wide frequency range. But for p-polarization, the angular range of high transmittance T_p (≈ 1) is much wider than

Optics EXPRESS

s-polarization apparently because of better wave impedance matching. So, based on this fact and implementability in engineering applications, the main cores which realize UWAHT can be summarized as follows: (i) For s-polarization, realization of high transission in the range of smaller incident angles ($[0°, 40°]$) through the anti-reflection property of dielectric substrate itself ($T_s \approx 1$), and realization of high transmission in the range of higher incident angles ($[40°, 90°]$) through the metasurface structures. (ii) But for p-polarization, we can only improve the transmittance T_p in the narrow range of large incident angle ($[70°, 90°]$) by metasurface structures, and utilize the anti-reflection property in the wide range of smaller incident angles ($[0°, 70°]$). And in some application scenarios, the angular range of high transmission does not have to ultra-wide (near grazing incidence). For this requirement, we can only modulate the s-polarization and utilize the wide angular range of p-polarized anti-reflection property.

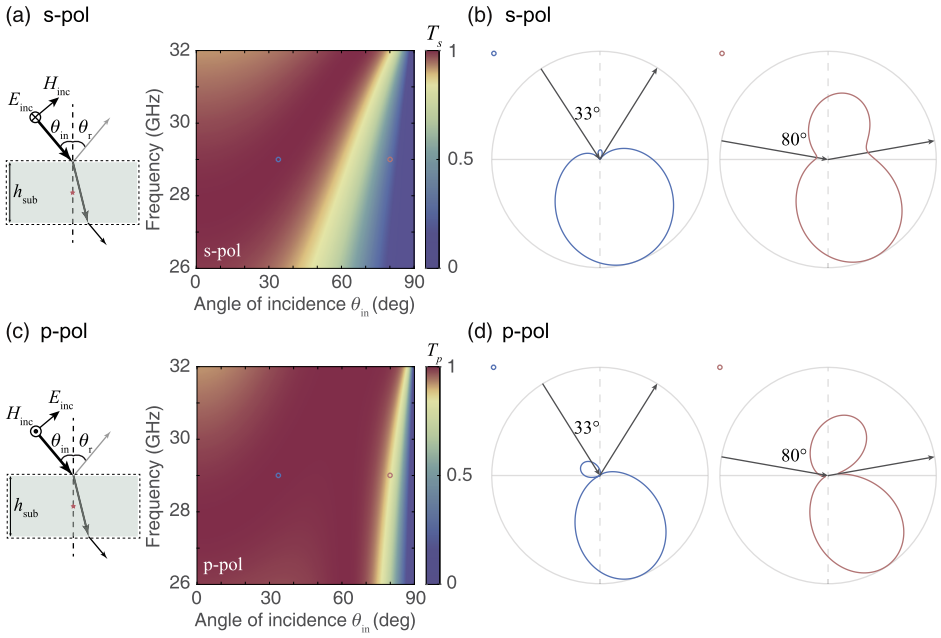

Fig. 1. The dual-polarized transmission property, and electric far-field patterns of dielectric substrate at specific incident angles. (a),(c) The dual-polarized transmittance T_s and T_p as a function of frequency and incident angle θ_{in}. The left insets show that the processes of different polarized EM wave impinges onto the single-layer substrate (the reflected wave vectors in substrate aren't shown in the insets). The height h_{sub} is 3 mm, relative permittivity ε_r is 3.27, loss tan δ is 0. (b),(d) The electric far-field patterns of substrate in one unit cell (the part in dashed boxes of left insets) by multipolar expansion when dual-polarized EM plane wave impinges at specific incident angle $\theta_{\text{in}} = 33°, 80°$. The corresponding blue and red circles are marked in the left transmittance angle-spectrums at frequency $f = 29$ GHz. The origins of multipolar expansion are marked by pale red pentagrams in the left insets. The directions of incidence and reflection are indicated by the black arrows.

Next, we will utilize the multipolar expansion method to analyze the multipolar components when the structures are excited by incident EM plane wave [53,55,56]. Through full-wave simulation software CMOSOL Multiphysics, we can obtain the electric field distribution $\boldsymbol{E}(\boldsymbol{r})$ in one unit cell. And then, the corresponding electric polarization currents can be described by:

$$\mathbf{J}(\mathbf{r}) = -i\omega\varepsilon_0 \left[\varepsilon_r(\mathbf{r}) - \varepsilon_{r,d}(\mathbf{r})\right] \mathbf{E}(\mathbf{r}), \tag{1}$$

Optics EXPRESS

where $\varepsilon_r(\mathbf{r})$ denotes the permittivity distribution, $\varepsilon_{r,d}(\mathbf{r})$ is the permittivity of the background medium, ε_0 is vacuum relative permittivity and ω is angular frequency. And then, the multipolar coefficients a_{lm} and b_{lm} can be expressed by:

$$\begin{aligned} a_{lm} &= \frac{(-i)^{l-1}k^2\eta O_{lm}}{E_0\sqrt{\pi(2l+1)}}\int \mathbf{J}(\mathbf{r})\cdot\mathbf{N}_{lm}^{(1)*}d^3r, \\ b_{lm} &= \frac{(-i)^{l+1}k^2\eta O_{lm}}{E_0\sqrt{\pi(2l+1)}}\int \mathbf{J}(\mathbf{r})\cdot\mathbf{M}_{lm}^{(1)*}d^3r \end{aligned} \tag{2}$$

where η is the vacuum impendence, $O_{lm} = \frac{1}{\sqrt{l(l+1)}}\sqrt{\frac{2l+1}{4\pi}\frac{(l-m)!}{(l+m)!}}$ ($l = 1, 2, 3, \ldots$ and $m = -l, -l+1, \ldots, 0, \ldots, l-1, l$), the integration is performed within the unit cell region V, and $\mathbf{N}_{lm}^{(1)}$, $\mathbf{M}_{lm}^{(1)}$ are vector spherical harmonic functions, where the superscript (1) denotes the first kind of spherical Bessel functions. a_{1m} expresses electric dipole (ED), a_{2m} expresses electric quadrupole (EQ), b_{1m} expresses magnetic dipole (MD), and b_{2m} expresses magnetic quadrupole (MQ). Through the expansion coefficients a_{lm} and b_{lm}, the radiated electric scatter field of single unit cell can be presented as follows:

$$\mathbf{E}_s(r,\theta,\phi) = \sum_{l=1}^{\infty}\sum_{m=-l}^{l} E_{lm}\left[a_{lm}\mathbf{N}_{lm}^{(3)} + b_{lm}\mathbf{M}_{lm}^{(3)}\right], \tag{3}$$

where $E_{lm} = E_0\frac{i^{l+1}(2l+1)}{2}\sqrt{\frac{(l-m)!}{l(l+1)(l+m)!}}$, where the superscript (3) denotes the third kind of spherical Bessel functions.

Using the above method, the radiated electric far-field $\boldsymbol{E}_f(r,\theta,\varphi)$ (r is big enough) of one unit cell of dielectric substrate which is shown in Fig. 1 (a)(c) can be obtained for any incident angles and frequency points. As shown in Fig. 1 (b) and (d), there is a obvious dip at the each reflected direction for $\theta_{\text{in}} = 33°$ due to totally anti-reflection property ($T_s, T_p = 1$), that is, KE is realized at this direction. But for $\theta_{\text{in}} = 80°$, the dips almost disappear at the reflected direction, which is corresponding to the low transmittance T_s or T_p. This inspires us that the UWAHT will be obtained when the added metallic metasurface structure and original substrate together achieve KE at any reflected directions in one unit cell.

So combining with the available and different anti-reflection properties of s- or p-polarization, the most practical modulated method is that the two polarizations can be individually modulated by different structures, and these structures have no multual interference. To our knowledge, the planar ring-like structures can be excited as similar vertical MD when EM plane wave impinges from any incident planes, which maybe have totally different responses for different polarizations. In Ref. [56], the S-ring periodic structures were proposed to realize random generalized Brewster effect, which can show good impedance match property in the large range of incident angle (near grazing incidence especially). To express the general multipolar properties of this structure, the planar S-ring periodic array was simulated by COMSOL. And the current density and multipolar components of single S-ring can be shown in Fig. 2. In Fig. 2 (a), when s-polarized EM wave impinges onto the planar S-ring metasurface in different incident planes ($\varphi = 0°, \varphi = 45°, \varphi = 90°$), the electric current density of the S ring rotates in the same direction around centers of the two half-rings, respectively, resulting in strong MD component. However, the intensity of ED is very weak because of the reverse direction of the electric current density. Thus, the total multipolar component of this structure is almost z-axis MD. But for p-polarized situation, as show in Fig. 2 (b), the major part of electric current density of the S-ring rotates in the reverse direction around centers of the two half-rings, respectively, resulting in a counteracted induced magnetic field of the two half-rings. Owing to the weak electric current density, the

Optics EXPRESS

electric dipole components are also weak. The corresponding results of multipolar decomposition of S-ring can also demonstrate the deductions which are shown in Fig. 2.

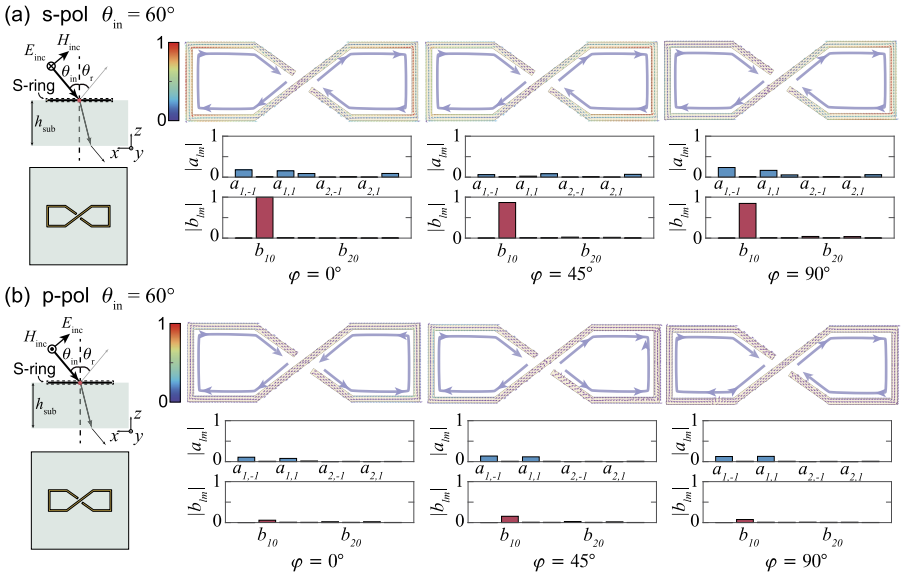

Fig. 2. The general interpretations of planar S-ring structure properties when s- or p-polarization plane wave impinges onto the metasurface at $\theta_{in} = 60°$ in different incident planes ($\varphi = 0°, \varphi = 45°, \varphi = 90°$). The definitions of corner marks *lm* can be found in the Section 2. The rotated directions of electric current density are marked by purple arrows in each half-ring. (a) For s-polarized EM wave, the current density and normalized multipolar decomposition results of S-ring structure in one unit cell. (b) For p-polarized EM wave, the current density and normalized multipolar decomposition results of S-ring structure in one unit cell.

Thus we can find a good and special property of this planar S-ring array, that is, it can modulate the s-polarized plane wave and has hardly any responses for p-polarization at appropriate frequency for any incident planes. In addition, when the S-ring structure is perpendicular to substrate surface, the magnetic field vector of p-polarized incident wave will be parallel to the equivalent MD direction of this structure, resulting in the predictable modulations of p-polarization. And another characteristic is that it shows z-axis MD responses in different incident planes ($\varphi = 0°, \varphi = 45°, \varphi = 90°$) for s-polarization. This kind of MD has high degree of symmetry in $x - y$ plane, resulting in similar responses in different incident planes easier. And it shows hardly any responses for p-polarization. Based on the two features of S-ring structure, two kinds of metasurfaces A and B were designed to realize dual-polarized UWAHT and WAHT, which were shown in Section 3.1 and Section 3.2 respectively.

3. Metasurface structures and simulated results

3.1. Dual-polarized UWAHT metasurface

This section describes the UWAHT metasurface, and the analysis of the near-full-transmission phenomenon through the multipolar expansion method based on the all-angle KE. As shown in Fig. 3(a), through the ideas and analysis in Section 2, a metasurface consisting of planar and vertical S-ring periodic structures and a dielectric substrate was designed. The s- or p-polarized EM plane wave can propagate through the metasurface at any incident angle θ_{in}. The details of this structure are presented in Fig. 3(b). It is notable that a part of the vertical S-ring array is buried

Optics EXPRESS

in the substrate. To eliminate the influence of loss, the structures in this study were designed in the microwave band, and the dielectric substrates were lossless. The relative permittivity of the substrate was $\varepsilon_r = 3.27$, and the height was $h_{sub} = 3$ mm. The other structural parameters were designed with $d_{x1} = d_{x3} = 0.5$ mm, $d_{x2} = d_{x4} = 0.7$ mm, $d_y = 0.8$ mm, $w = 0.05$ mm, and $d_y = d_z = 0.8$ mm.

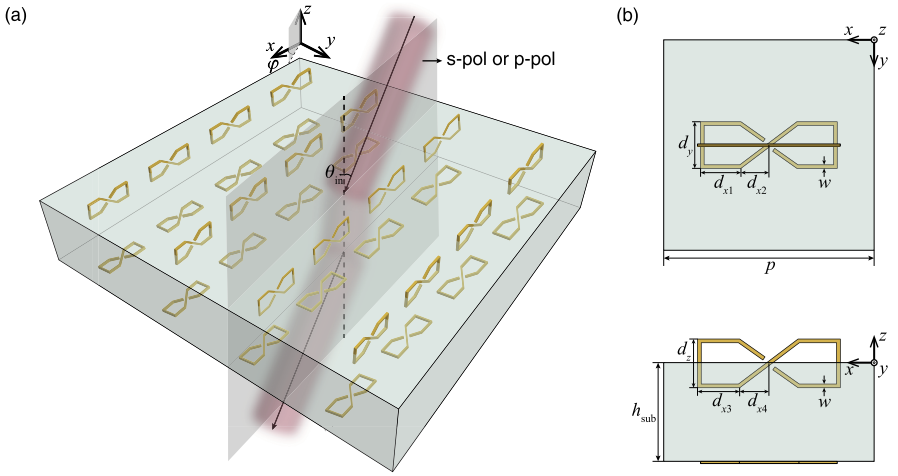

Fig. 3. Schematic of the S-ring UWAHT metasurface. (a) The planar S-ring periodic structures are placed on the bottom of the substrate, and the vertical S-ring periodic structures are placed on the top of the substrate. (b) Top view and front view of one unit cell of the metasurface.

When s- or p-polarized EM plane wave impinging onto the metasurface, as shown in Fig. 3(a) in the incident plane $\varphi = 0°$, the simulated results are shown in Fig. 4. As shown in Fig. 4(a), T_s can be close to unity up to an incident angle θ_{in} of almost 90° at frequency $f = 28.36$ GHz; that is, UWAHT can be realized at this frequency. As shown in Fig. 4(b), unlike the s-polarized situation, the vertical S-ring array can be excited to realize near-full transmission up to near-grazing incidence at the same frequency. For the two different polarizations, the relationship between the transmittance and incident angle θ_{in} is shown in Fig. 4(c). Clearly, the transmittance of the two polarizations approaches 98% up to grazing incidence at a frequency of $f = 28.36$ GHz.

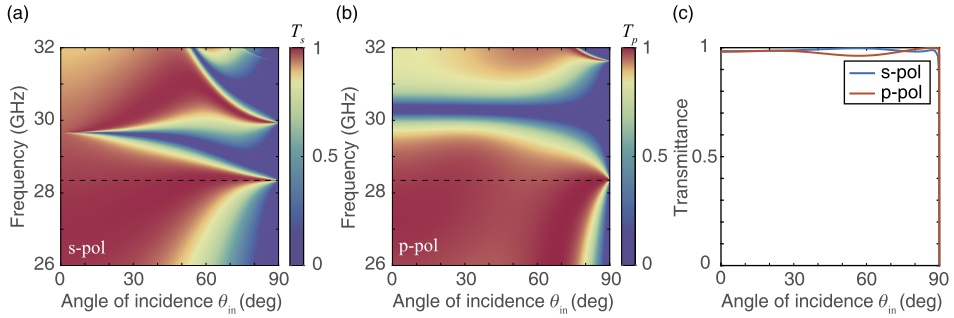

Fig. 4. Simulated results of the metasurface shown in Fig. 3. (a), (b) Transmittance T_s and T_p as a function of the incident angle θ_{in} and frequency when the s- or p-polarized plane wave impinges in the incident plane $\varphi = 0°$. (c) Transmittance as a function of incident angle θ_{in} at frequency $f = 28.36$ GHz, which corresponds to the black dashed line shown in (a) and (b) for the two polarizations.

Optics EXPRESS

The results of multipolar expansions for s- or p-polarized situations as shown in Fig. 4(c). For the s-polarized situation, as shown in the upper half of Fig. 5(a), the multipolar expansion results of the planar S-ring structure show that the MD component gradually increases as the incident angle θ_{in} increases. In the lower half of Fig. 5(a), the multipolar expansion results of the substrate in one unit cell show that other-ordered multipolar components exist in addition to the basic ED. It should be noted that these non-ED responses, that is, MD, EQ, and MQ, are mainly due to the larger ratio of thickness h_{sub} and incident wavelength λ_0 and the selection of origins. To better demonstrate the real multipolar components of the S-ring structure, the center of the S-ring was selected as the origin. Then, the electric far-field patterns for different incident angles $\theta_{in} = 20°, 40°, 60°, 70°, 80°, 85°$, as shown in Fig. 5(b), exhibit a dip in the reflected direction (black dashed arrows). The far-field patterns of the S-ring structure and substrate in this unit cell intersect at six different reflected directions. It is notable that the effect of the metasurface structure pattern on the total radiated pattern is small when the incident angle $\theta_{in}<60°$. Therefore, in this incident-angle range, the ordinary anti-reflection of the substrate plays a dominant role. Then, as the MD component of the structure increases, satisfaction of the KE condition is mainly determined by the metasurface structure. This result clearly explains that the destructive interference of the near-MD-responsive S-ring metasurface and substrate can satisfy the condition of all-angle KE to realize UWAHT. The full-wave simulated electric field E_y distributions that correspond to the six different incident angles θ_{in} are shown beside the far-field patterns. First, almost no reflection is observed, owing to the almost equal intensity of the incident and transmitted waves. Second, through the observation of local electric near-field distributions around the metasurface, the planar S-ring structure is strongly excited, and the vertical S-ring structure has no response.

For the p-polarized situation, as shown in the upper half of Fig. 5(c), the multipolar expansion results of the vertical S-ring show that the ED component is almost as strong as the MD component. The generation of the ED component is mainly due to the excitation of the p-polarized EM plane wave and modulation of the finite-thickness substrate. As shown in the lower half of Fig. 5(c), the ED component is the strongest, and other non-ED components can also be obtained for the same reason as in the s-polarized situation. As shown in Fig. 5(d), similar to s-polarization, an obvious dip can be observed in the reflected direction of each total far-field pattern. The magnetic field H_y distributions are shown in Fig. 5(d), which shows a near-full transmission for the six different incident angles. Unlike s-polarization, the local near-field of the vertical S-ring is quite strong, and the planar S-ring has no response. This is the main reason why only the planar S-ring structure was analyzed for the s-polarization situation, and only the vertical S-ring structure was analyzed for the p-polarization situation.

The current density and normalized multipolar decomposition histograms of vertical and planar S-rings at incident angle $\theta_{in} = 60°, 80°$ were shown in Fig. 6 respectively. Apparently, for the planar S-ring, the strong z-axis MD component can be excited by s-polarized EM wave, and a little ED component can be excited by p-polarized EM wave (ED is too weak to be ignored). For the vertical S-ring, the MD component in the $x-y$ plane is strong and ED component is also a little strong because of the unequal electric current density in the two half-rings when p-polarized wave illuminates. And the responses are very weak when s-polarized wave illuminates. Combined with the electric-field distributions shown in Fig. 5(b) and (d), these results clearly show that modulations of these two structures for the two polarizations are totally independent.

The discussions of simulated results have not considered loss in this paper. But a very important and helpful conclusion is that the first Kerker condition will be inhibited when the loss is not zero [57]. So we analyzed the impacts of loss in dielectric substrate by full-wave simulation software for the s-polarized situation which is shown in Fig. 3. As shown in Fig. 7, when the loss tangent $\tan\delta$ is set as different values ($\tan\delta = 0.001, 0.01, 0.05, 0.1$), we can obtain the transmission spectrums and total electric radiated patterns in one unit cell at specific incident

Optics EXPRESS

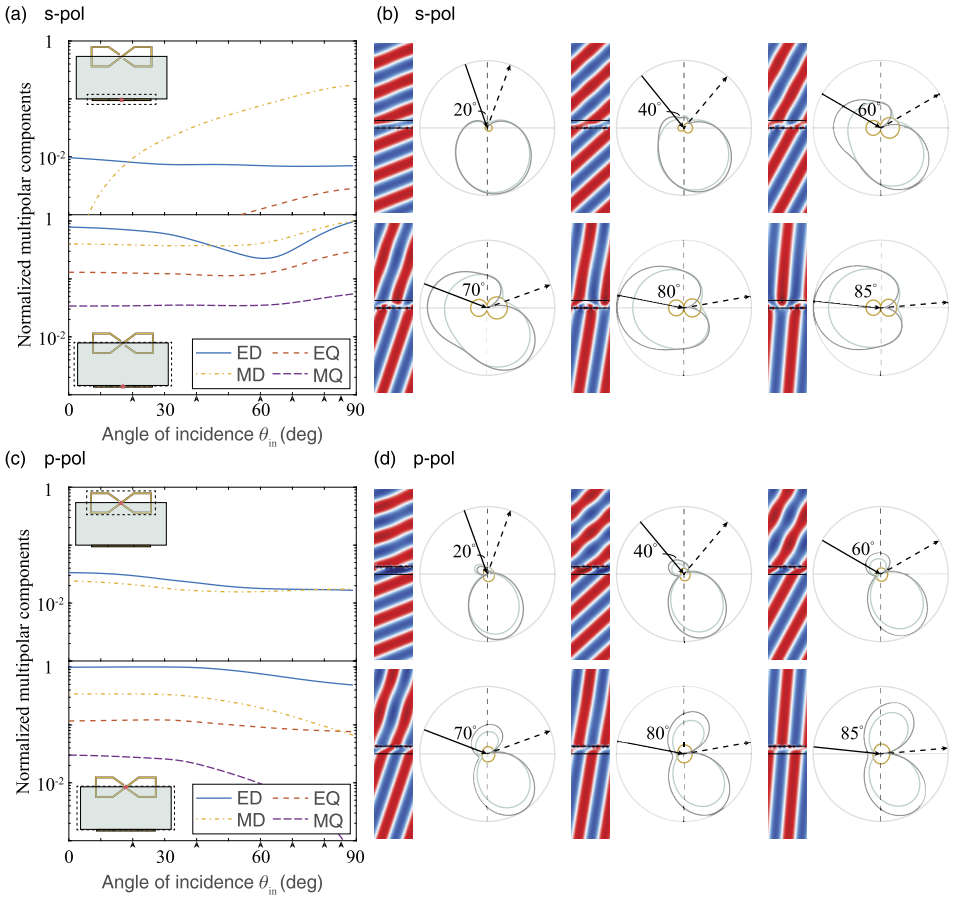

Fig. 5. Numerical results of the multipolar expansion and full-wave simulated results of the electric field and magnetic field distributions at frequency $f = 28.36$ GHz, as shown in Fig. 4. For the two different polarized situations, all multipolar components were normalized, and the logarithm was taken. The origin of the multipolar expansion is the center of the S-ring (planar S-ring for the s-polarization situation, and vertical S-ring for the p-polarization situation; the origins are shown in (a) and (c) using pale red pentagrams) in one unit cell. (a), (c) Normalized multipolar components of the substrate and metal structures in one unit cell as a function of incident angle θ_{in} for the two different polarizations, respectively. (b), (d) Electric radiated far-field patterns in one unit cell (light brown patterns represent structures, light green patterns represent substrates, and gray lines represent total patterns) and the simulated results of the electric and magnetic field (E_y for s-polarization, and H_y for p-polarization) distributions for incident angles $\theta_{in} = 20°, 40°, 60°, 70°, 80°, 85°$ (black arrowheads in Fig. 4(a) and (c)) respectively. The directions of incidence and reflection are indicated by the black arrows.

Optics EXPRESS

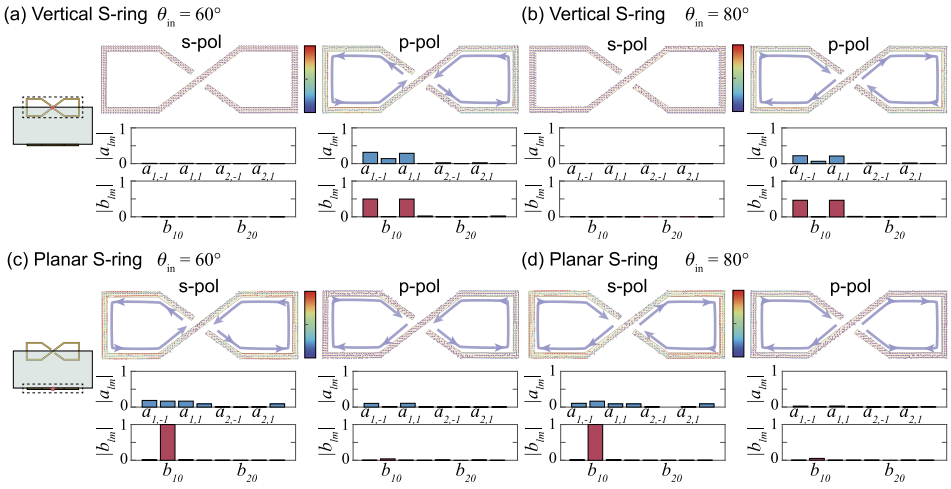

Fig. 6. The simulated current density and normalized multipolar decomposition of vertical and planar S-ring structures as shown in Fig. 3 when s- or p-polarized plane wave impinges onto the metasurface at $\theta_{in} = 60°, 80°$. The rotated directions of electric current density are marked by purple arrows in each half-rings. (a),(b) The simulated results of vertical S-ring at $\theta_{in} = 60°, 80°$ for the two polarizations. (c),(d) The simulated results of planar S-ring at $\theta_{in} = 60°, 80°$ for the two polarizations.

angle ($\theta_{in} = 60°, 80°$) and frequency. Apparently, the transmittance T_s will get lower in the whole range of frequency and angle when loss tangent $\tan\delta$ gets bigger. When the specific frequency points are selected (marked by the gray dashed lines in the frequency angle-spectrums), we can get four curves as shown in the middle column of Fig. 7. Even if the loss tangent $\tan\delta$ is 0.001, the transmittance T_s has obvious declines in the range of larger incident angle. And for the specific incident angles $\theta_{in} = 60°, 80°$, the dips will disappear at reflected directions gradually as $\tan\delta$ gets bigger, which can demonstrate the loss can affect the realizations of KE. In order to eliminate the impacts of loss furthest, we will use the ultra-low loss Rogers dielectric substrate and quartz glass to perform experiments.

3.2. *Near-isotropic metasurface as a 5G mmWave communication electromagnetic window*

Except for the dual-polarized UWAHT which is shown in Section 3.1, based on the analysis in the end of Section 2, we can also modulate the transmission of s-polarization by a metasurface and utilize the good transmittance property of p-polarization to realize almost the same WAHT in different incident planes. The S-ring structure which is shown in Fig. 2 has similar responses when s-polarized EM plane wave impinges in different incident planes $\varphi = 0°, 45°, 90°$, which can be equivalent to strong z-axis MD by multipolar decomposition method. But apparently, the modulated frequency point is not identical in different incident planes because this structure itself has only C_2 symmetry. To achieve the same responses in different incident planes as far as possible, a relatively natural method is the improvement of symmetry, such as, C_2 transforms to C_4 and so on. So as shown in the inset of Fig. 8 (a), the first step is translating the S-ring to another surface of substrate along z-axis. We can find apparent difference of transmittance spectrums when EM wave impinges from the same incident direction in different incident planes $\varphi = 0°$ and $\varphi = 45°$. It is noting that the rotational symmetry has bigger impacts for this target. So the rotational angle α of S-ring around center can be a degree of freedom to adjust the symmetry of the whole unit cell. As shown in Fig. 8 (a)-(e), α has been changed from

Optics EXPRESS

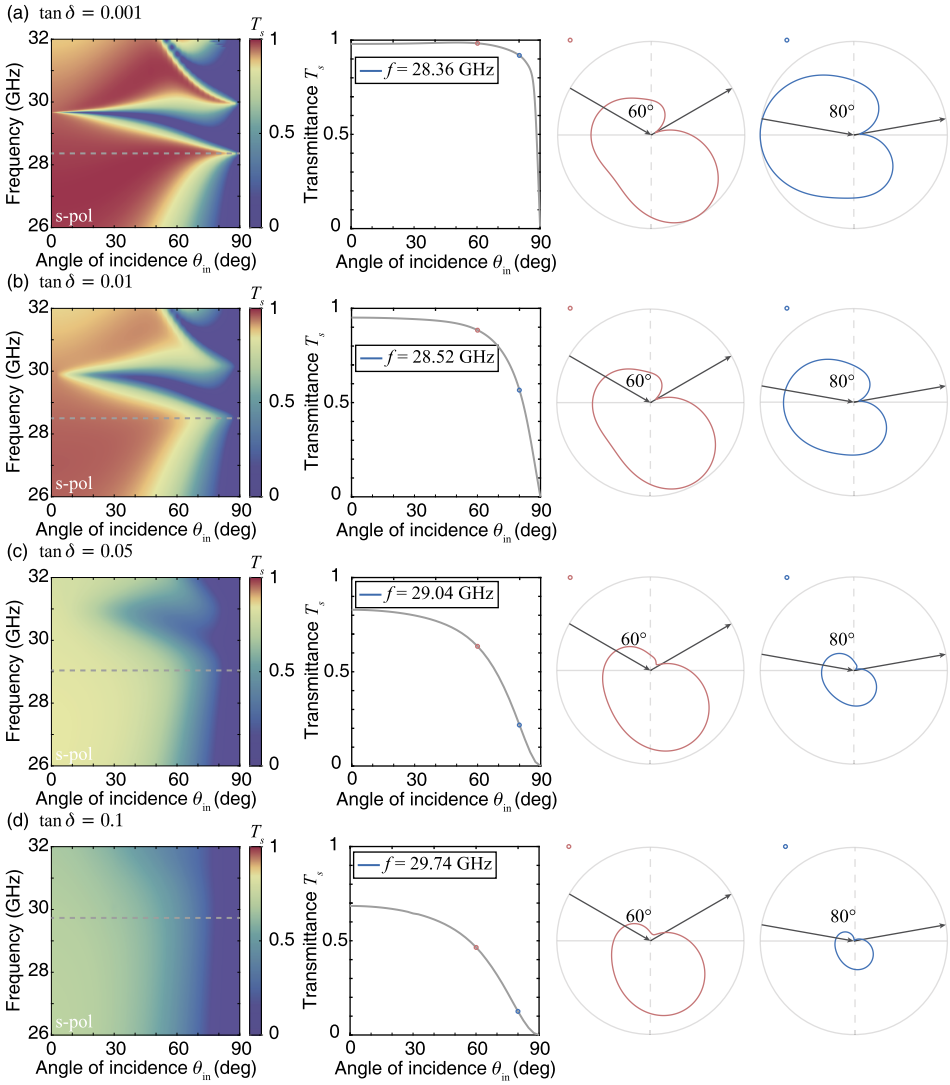

Fig. 7. The comparsions of transmission spectrums and corresponding total electric radiated patterns in one unit cell at incident angle $\theta_{\text{in}} = 60°, 80°$, which sets different loss tangent $\tan\delta = 0.001, 0.01, 0.05, 0.1$ of substrate for the s-polarized situation in the Fig. 3. The origin of multipolar decomposition is the center of substrate. (a) $\tan\delta = 0.001$. (b) $\tan\delta = 0.01$. (c) $\tan\delta = 0.05$. (d) $\tan\delta = 0.1$.

Optics EXPRESS

0° – 90°, resulting in the difference of transmittance spectrums gets smaller and smaller for different incident planes and same incident angle. And when α is 90°, that is, the structure has S_4 symmetry, the transmittance spectrums are almost coincident. Although there is a little difference at high frequency (f>28.7 GHz) due to the influence of high-ordered wave-guided modes, the structure has good near-isotropic transmission property which can be used in many practical engineering applications, such as 5G mmWave communication. As an example, to reduce backscattered attenuation of 5G mmWave signals from base stations to indoor terminals, metasurfaces can be installed on the external glazed windows and walls of buildings, which can be called EMWs. As shown in Fig. 9(a), the EMW can realize near-full-transmission for 5G mmWave signals that come from any direction. Therefore, the near-isotropic responses of the metasurface, which means that periodic structures have the same properties for any-direction EM waves, are highly important.

As shown in Fig. 9(b), a new S-ring metasurface B was designed. The simulated results for the near-isotropic S-ring metasurface are shown in Fig. 10. As shown in Fig. 10(a), (d) and (b), (e), the transmittance spectra are almost identical when the s- or p-polarization EM plane wave impinges with different incident planes $\varphi = 0°$ and $\varphi = 45°$. This result can explain the near-isotropy of the S-ring metasurface. As shown in Fig. 10(b) and (e), the transmission of p-polarized EM plane waves are affected little by the periodic structures and can be modulated only by the properties of the dielectric substrate. As shown in Fig. 10(c) and (f), the transmittance of s-polarization is approximately 97% up to grazing incidence at a frequency of $f = 27.83$ GHz. The transmittance of p-polarization is larger than 90% for incident angle $\theta_{in} \leq 80°$.

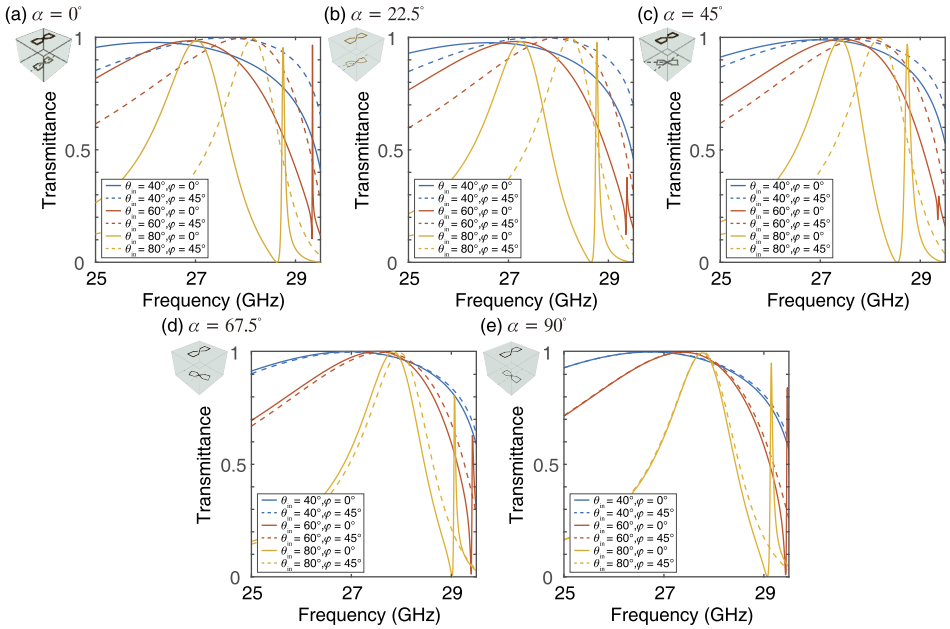

Fig. 8. When the rotating angle α is changed from 0° to 90°, the comparsions of s-polarized transmittance spectrums in incident planes $\varphi = 0°, 45°$ at incident angle $\theta_{in} = 40°, 60°, 80°$. The solid lines represent $\varphi = 0°$, and the dashed lines represent $\varphi = 45°$. (a) $\alpha = 0°$. (b) $\alpha = 22.5°$. (c) $\alpha = 45°$. (d) $\alpha = 67.5°$. (e) $\alpha = 90°$.

To further discuss the near-isotropy of the metasurface B, the results of multipolar decomposition and current density have been shown. As shown in Fig. 11, for the two incident planes ($\varphi = 0°, 45°$), the normalized multipolar components of metasurface in one unit cell (S-rings and substrate) as a function of incident angle can be obtained through multipolar decomposition. Apparently,

Optics EXPRESS

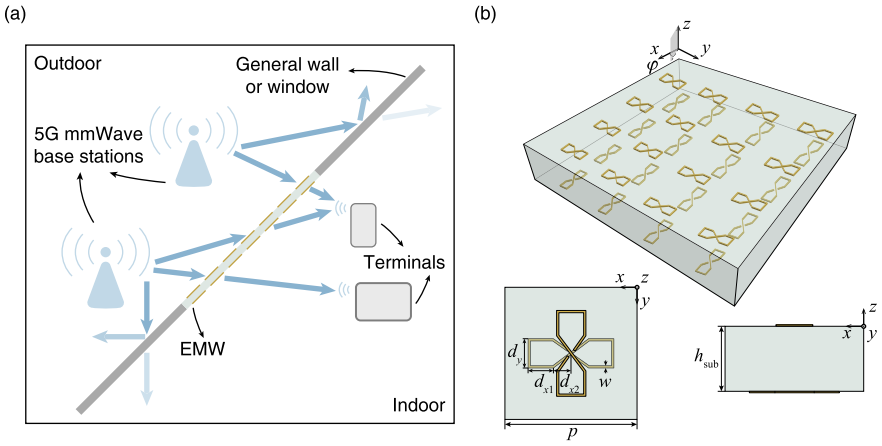

Fig. 9. Schematic of EMW applications and near-isotropic UWAHT metasurface. (a) Schematic of the applied EMW scenarios, realizing EM wave full-transmission from outdoor 5G base stations into the room. The shades of the blue arrows indicate the intensity of the propagated signal. (b) Schematic of the near-isotropic UWAHT metasurface EMW.

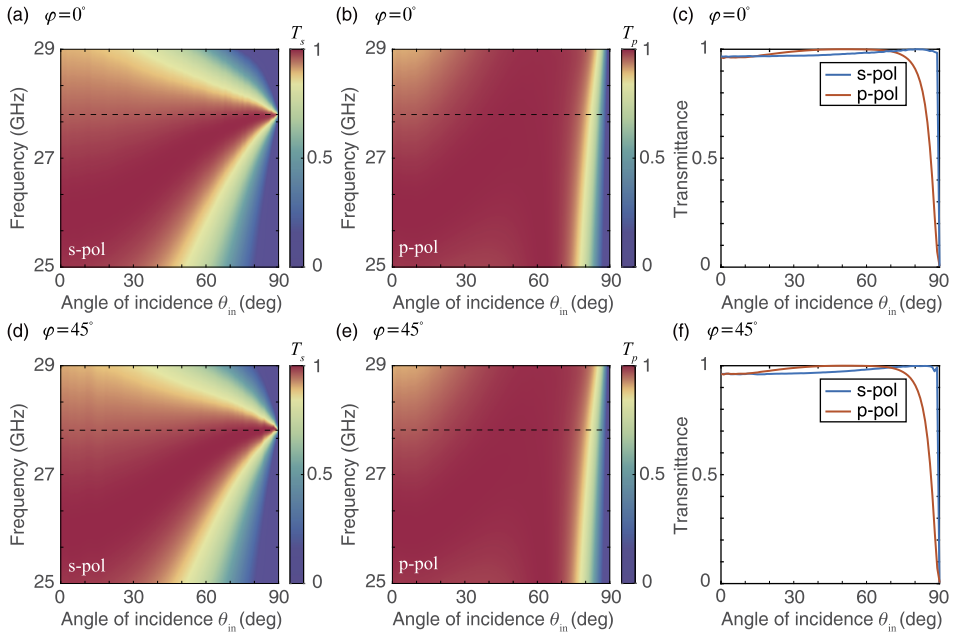

Fig. 10. Simulated results of a near-isotropic s-polarized UWAHT metasurface. (a), (d) The s-polarized transmittance T_s as a function of the incident angle θ_{in} and frequency for $\varphi = 0°$ and $\varphi = 45°$, respectively. (b), (e) The p-polarized transmittance T_p as a function of the incident angle θ_{in} and frequency for $\varphi = 0°$ and $\varphi = 45°$, respectively. (c), (f) The transmittance as a function of the incident angle θ_{in} for the two polarizations, respectively, at frequency $f = 27.83$ GHz of realization of near-isotropic s-polarized UWAHT, which is corresponding to the black dashed lines in (a), (b) and (d), (e).

Optics EXPRESS

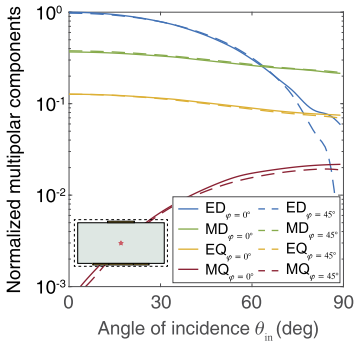

Fig. 11. The normalized multipolar decomposition results of S-rings and substrate in one unit cell as a function of incident angle θ_{in} in incident planes $\varphi = 0°, 45°$ for the s-polarized situation as shown in Fig. 9 (b).

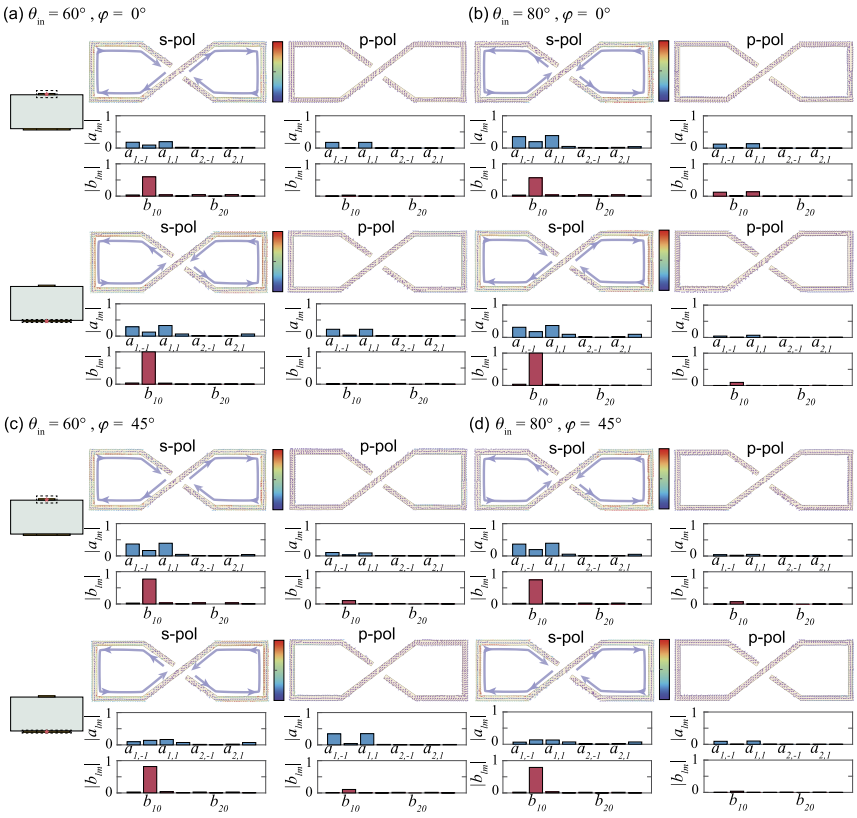

Fig. 12. The simulated current density and normalized multipolar decomposition of S-ring structures on the top and bottom of substrate as shown in Fig. 9 (b) when s- or p-polarized plane wave impinges onto the metasurface at $\theta_{\text{in}} = 60°, 80°$ in incident planes $\varphi = 0°, 45°$. The rotated directions of electric current density are marked by purple arrows in each half-ring. (a),(b) The respective simulated results of S-rings on the top and bottom of substrate at $\theta_{\text{in}} = 60°, 80°$ in incident plane $\varphi = 0°$ for the two polarizations. (c),(d) The respective simulated results of S-rings on the top and bottom of substrate at $\theta_{\text{in}} = 60°, 80°$ in incident plane $\varphi = 45°$ for the two polarizations.

Optics EXPRESS

the solid lines and dashed lines are almost coincident, except the ED components have some difference when incident angle θ_{in}>75°. But in fact, the intensity of ED gets weaker and weaker, resulting in few impacts for transmission. So when s-polarized wave impinges in different incident planes, the metasurface has almost identical multipolar responses at any incident angles, which can give rise to almost the same transmission property. Next the electric current density and multipolar components at the incident angle $\theta_{in} = 60°, 80°$ in different incident planes can be obtained. As shown in Fig. 12, for p-polarization, the two S-ring structures have a little responses in incident planes $\varphi = 0°, 45°$, which can be expressed as weak ED components through multipolar decomposition. There is few modulations to p-polarized EM wave. So the spectrums of transmittance T_p in each incident plane are from interference of the dielectric substrate itself. For s-polarization, the flow direction of electric current density is similar for the two S-rings, resulting in the strong z-axis MD in different incident angles and planes. It is noting that the weak ED component is caused by different electric current density intensity of the two half-rings.

4. Experimental verification

As shown in Fig. 13(a), the experimental instruments were designed to measure the transmittance. Two horn antennas were fixed and connected to a vector network analyzer (Keysight N5245B). The centers of the samples and horns were collinear. Absorbent materials were installed around the samples. The samples could rotate along the z-axis, and the rotated angle θ was considered as the incident angle θ_{in}. As shown in Fig. 13(b), two types of samples were fabricated. The top surface of sample I is shown at the top of Fig. 13(b). A planar copper S-ring array was printed on the top of the PCB substrate (relative permittivity $\varepsilon_{r1} = 3.27$, loss tangent $\tan\delta_1 = 0.002$, height $h_{PCB} = 3$ mm, size 22 cm × 22 cm, and number of unit cells 46 × 46). The bottom surface of sample I is shown in the middle of Fig. 13(b). One-dimensional periodic long grooves (width $w_{grooves} = 0.5$ mm, depth $h_{grooves} = 0.1$ mm) were fabricated on the bottom of the substrate. Vertical S-ring structures that were printed on the surface of the dielectric long strips (Rogers RT / duroid 5880, relative permittivity $\varepsilon_{r2} = 2.2$, loss tangent $\tan\delta_2 = 0.0009$, thickness $t_{strips} = 0.5$ mm, and width $w_{strips} = 1$ mm) can be inserted in the long grooves exactly. Sample II is shown at the bottom of Fig. 13(b). The copper S-ring structures B were printed on the two surfaces of quartz glass (relative permittivity $\varepsilon_{r3} = 3.79$ in the mmWave band, loss tangent $\tan\delta_3 = 0.001$, height $h_{glass} = 2.97$ mm, and size of each piece 10 cm × 10 cm) using the photolithography method. Owing to the limitations of the photolithography method, the final sample II was composed of four square samples.

The s- and p-polarized experimental results of sample I at the incident plane $\varphi = 0°$ are shown in Fig. 13(c). The s-polarized transmission transmittance $T_s \geq 80\%$ near $f = 28.37$ GHz up to $\theta_{in} = 80°$ at the two incident planes. The p-polarized transmission coefficient $T_p \geq 80\%$ for $f = 26 - 29.5$ GHz up to $\theta_{in} = 80°$. The s- and p-polarized experimental results of sample II at the incident plane $\varphi = 0°$ and $\varphi = 45°$ are shown in Fig. 13(d) and (e). The s-polarized transmittance $T_s \geq 80\%$ near $f = 28$ GHz up to $\theta_{in} = 80°$ for the two incident planes. The p-polarized transmittance T_p was also greater than 80% in the entire tested frequency domain $f = 26 - 29$ GHz, which shows ordinary anti-reflection properties by the dielectric substrate itself. Clearly, sample II has the same transmittance property in different incident planes, which verifies the near-isotropy of this metasurface. These results also show the excellent potential applications of this metasurface EMW.

Optics EXPRESS

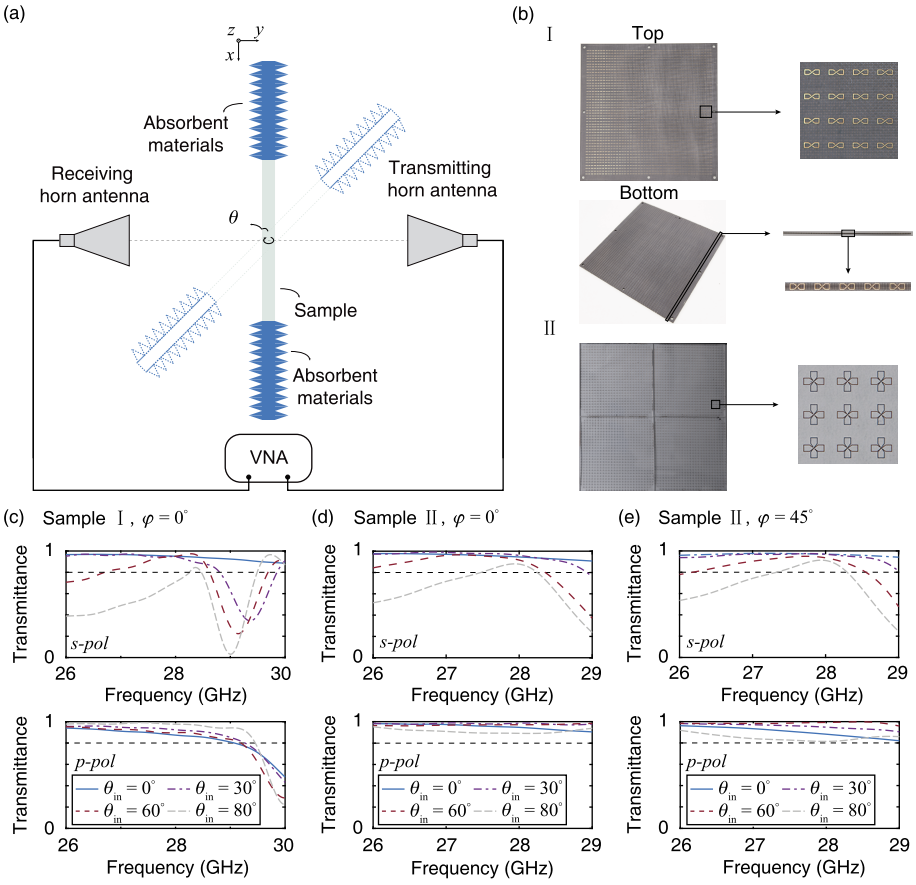

Fig. 13. Schematics of the experimental instruments, samples, and results. (a) Schematic of the experimental instruments. (b) Detailed photographs of the two samples. I: Dual-polarized UWAHT S-ring metasurface; II: near-isotropic 5G mmWave EMW metasurface. (c) Experimental results of sample I at the incident plane $\varphi = 0°$. Transmittance is 80% which is indicated by a black dashed line. (d) Experimental results of sample II at the incident plane $\varphi = 0°$. (e) Experimental results of sample II at the incident plane $\varphi = 45°$.

5. Conclusion

In summary, on the basis of the all-angle KE, two metasurfaces that can realize UWAHT are proposed. First, an S-ring metasurface was designed to realize almost full transmission up to grazing incidence for the two polarized EM plane waves. The UWAHT of this metasurface was analyzed using the multipolar expansion method. Second, in order to connect this effect with actual applications, a new near-isotropic S-ring metasurface was designed as a 5G mmWave communication EMW, which can realize almost full transmission until grazing incidence for s-polarization and transmittance larger than 90% at incident angle $\theta_{in} \leq 80°$ for p-polarization. It should be noted that the core of our method is individual modulations for different polarizations and incident angles. The experiments were performed using a microwave test system. The results show the excellent transmittance properties of the two metasurfaces. We believe that this work will enable the design and fabrication of easy-to-integrate KE metasurface devices and connect the KE with practical applications in many scenarios.

Funding. National Key Research and Development Program of China (2020YFB1806405, 2021YFA1400603);

Optics EXPRESS

National Natural Science Foundation of China (11727811, 91750102, 91963212); Science and Technology Commission of Shanghai Municipality (19DZ2253000, 19XD1434600, 2019SHZDZX01).

Disclosures. The authors declare no conflicts of interest.

Data availability. Data underlying the results presented in this paper are not publicly available at this time but may be obtained from the authors upon reasonable request.

References

1. L. Novotny and B. Hecht, *Principles of nano-optics* (Cambridge University, Cambridge, England, 2012).
2. J. A. Gordon, C. L. Holloway, and A. Dienstfrey, "A physical explanation of angle-independent reflection and transmission properties of metafilms/metasurfaces," Antennas Wirel. Propag. Lett. **8**, 1127–1130 (2009).
3. Y. He and G. V. Eleftheriades, "A thin double-mesh metamaterial radome for wide-angle and broadband applications at millimeter-wave frequencies," IEEE Trans. Antennas Propag. **68**(3), 2176–2185 (2019).
4. C. Jin, Q. Lv, B. Zhang, J. Liu, S. An, Z. S. He, and Z. Shen, "Ultra-wide-angle bandpass frequency selective surface," IEEE Trans. Antennas Propag. **69**(9), 5673–5681 (2021).
5. H. Chen, H. Chen, X. Xiu, Q. Xue, and W. Che, "Transparent fss on glass window for signal selection of 5g millimeter wave communication," Antennas Wirel. Propag. Lett. **20**(12), 2319–2323 (2021).
6. J. B. Pendry, D. Schurig, and D. R. Smith, "Controlling electromagnetic fields," Science **312**(5781), 1780–1782 (2006).
7. R. Liu, C. Ji, J. Mock, J. Chin, T. Cui, and D. Smith, "Broadband ground-plane cloak," Science **323**(5912), 366–369 (2009).
8. T. Ergin, N. Stenger, P. Brenner, J. B. Pendry, and M. Wegener, "Three-dimensional invisibility cloak at optical wavelengths," Science **328**(5976), 337–339 (2010).
9. H. F. Ma and T. J. Cui, "Three-dimensional broadband ground-plane cloak made of metamaterials," Nat. Commun. **1**(1), 21 (2010).
10. S. M. Kamali, E. Arbabi, A. Arbabi, Y. Horie, M. Faraji-Dana, and A. Faraon, "Angle-multiplexed metasurfaces: encoding independent wavefronts in a single metasurface under different illumination angles," Phys. Rev. X **7**(4), 041056 (2017).
11. E. Arbabi, A. Arbabi, S. M. Kamali, Y. Horie, and A. Faraon, "Multiwavelength polarization-insensitive lenses based on dielectric metasurfaces with meta-molecules," Optica **3**(6), 628–633 (2016).
12. V.-C. Su, C. H. Chu, G. Sun, and D. P. Tsai, "Advances in optical metasurfaces: fabrication and applications," Opt. Express **26**(10), 13148–13182 (2018).
13. K. J. Au, *Electromagnetic wave theory* (Wiley, Hoboken, NJ, USA, 1986).
14. N. I. Zheludev and Y. S. Kivshar, "From metamaterials to metadevices," Nat. Mater. **11**(11), 917–924 (2012).
15. T. J. Cui, M. Q. Qi, X. Wan, J. Zhao, and Q. Cheng, "Coding metamaterials, digital metamaterials and programmable metamaterials," Light: Sci. Appl. **3**(10), e218 (2014).
16. D. R. Smith, J. B. Pendry, and M. C. Wiltshire, "Metamaterials and negative refractive index," Science **305**(5685), 788–792 (2004).
17. C. Caloz, "Perspectives on em metamaterials," Mater. Today **12**(3), 12–20 (2009).
18. T. J. Cui, "Microwave metamaterials," Natl. Sci. Rev. **5**(2), 134–136 (2018).
19. N. Liu, H. Guo, L. Fu, S. Kaiser, H. Schweizer, and H. Giessen, "Three-dimensional photonic metamaterials at optical frequencies," Nat. Mater. **7**(1), 31–37 (2008).
20. J. Zhang, W. Liu, Z. Zhu, X. Yuan, and S. Qin, "Strong field enhancement and light-matter interactions with all-dielectric metamaterials based on split bar resonators," Opt. Express **22**(25), 30889–30898 (2014).
21. W. Liu and Y. S. Kivshar, "Multipolar interference effects in nanophotonics," Philos. Trans. R. Soc., A **375**(2090), 20160317 (2017).
22. V. G. Veselago, "Electrodynamics of substances with simultaneously negative and," Usp. Fiz. Nauk **92**(7), 517 (1967).
23. H. Wu, D. Kong, Z. Ruan, P.-C. Hsu, S. Wang, Z. Yu, T. J. Carney, L. Hu, S. Fan, and Y. Cui, "A transparent electrode based on a metal nanotrough network," Nat. Nanotechnol. **8**(6), 421–425 (2013).
24. Y. Lou, H. Pan, T. Zhu, and Z. Ruan, "Spatial coupled-mode theory for surface plasmon polariton excitation at metallic gratings," J. Opt. Soc. Am. B **33**(5), 819–824 (2016).
25. Z. Ruan and M. Qiu, "Enhanced transmission through periodic arrays of subwavelength holes: the role of localized waveguide resonances," Phys. Rev. Lett. **96**(23), 233901 (2006).
26. D. Lin, P. Fan, E. Hasman, and M. L. Brongersma, "Dielectric gradient metasurface optical elements," Science **345**(6194), 298–302 (2014).
27. H.-T. Chen, A. J. Taylor, and N. Yu, "A review of metasurfaces: physics and applications," Rep. Prog. Phys. **79**(7), 076401 (2016).
28. F. Ding, A. Pors, and S. I. Bozhevolnyi, "Gradient metasurfaces: a review of fundamentals and applications," Rep. Prog. Phys. **81**(2), 026401 (2017).
29. M. Chen, M. Kim, A. M. Wong, and G. V. Eleftheriades, "Huygens' metasurfaces from microwaves to optics: a review," Nanophotonics **7**(6), 1207–1231 (2018).

Optics EXPRESS

30. S. B. Glybovski, S. A. Tretyakov, P. A. Belov, Y. S. Kivshar, and C. R. Simovski, "Metasurfaces: From microwaves to visible," Phys. Rep. **634**, 1–72 (2016).
31. A. P. Slobozhanyuk, A. N. Poddubny, A. J. Raaijmakers, C. A. van den Berg, A. V. Kozachenko, I. A. Dubrovina, I. V. Melchakova, Y. S. Kivshar, and P. A. Belov, "Enhancement of magnetic resonance imaging with metasurfaces," Adv. Mater. **28**(9), 1832–1838 (2016).
32. J. Ma, F. Xie, W. Chen, J. Chen, W. Wu, W. Liu, Y. Chen, W. Cai, M. Ren, and J. Xu, "Nonlinear lithium niobate metasurfaces for second harmonic generation," Laser Photonics Rev. **15**(5), 2000521 (2021).
33. Y. Chen, Y. Zhang, and A. F. Koenderink, "General point dipole theory for periodic metasurfaces: magnetoelectric scattering lattices coupled to planar photonic structures," Opt. Express **25**(18), 21358–21378 (2017).
34. N. Yu and F. Capasso, "Flat optics with designer metasurfaces," Nat. Mater. **13**(2), 139–150 (2014).
35. P. Genevet, F. Capasso, F. Aieta, M. Khorasaninejad, and R. Devlin, "Recent advances in planar optics: from plasmonic to dielectric metasurfaces," Optica **4**(1), 139–152 (2017).
36. F. Aieta, M. A. Kats, P. Genevet, and F. Capasso, "Multiwavelength achromatic metasurfaces by dispersive phase compensation," Science **347**(6228), 1342–1345 (2015).
37. W. Liu, "Generalized magnetic mirrors," Phys. Rev. Lett. **119**(12), 123902 (2017).
38. C. L. Holloway, E. F. Kuester, J. A. Gordon, J. O'Hara, J. Booth, and D. R. Smith, "An overview of the theory and applications of metasurfaces: The two-dimensional equivalents of metamaterials," IEEE Antennas Propag. Mag. **54**(2), 10–35 (2012).
39. Z. Wu, M. Zhou, E. Khoram, B. Liu, and Z. Yu, "Neuromorphic metasurface," Photonics Res. **8**(1), 46–50 (2020).
40. T. Feng, A. A. Potapov, Z. Liang, and Y. Xu, "Huygens metasurfaces based on congener dipole excitations," Phys. Rev. Appl. **13**(2), 021002 (2020).
41. Z. Ma, H. Fan, H. Zhou, M. Huang, and J. Luo, "Broadband perfect transparency-to-absorption switching in tilted anisotropic metamaterials based on the anomalous brewster effect," Opt. Express **29**(24), 39186–39199 (2021).
42. M. Huang, X. Li, and J. Luo, "All-dielectric unidirectional complementary media for transmission enhancement," Opt. Express **28**(22), 33263–33273 (2020).
43. D. Van Labeke, D. Gérard, B. Guizal, F. I. Baida, and L. Li, "An angle-independent frequency selective surface in the optical range," Opt. Express **14**(25), 11945–11951 (2006).
44. D. Li, T.-W. Li, E.-P. Li, and Y.-J. Zhang, "A 2.5-d angularly stable frequency selective surface using via-based structure for 5g emi shielding," IEEE Trans. Electromagn. Compat. **60**(3), 768–775 (2017).
45. M. I. Khan, B. Hu, A. Amanat, N. Ullah, M. J. I. Khan, and A. R. Khalid, "Efficient asymmetric transmission for wide incidence angles using bi-layered chiral metasurface," J. Phys. D: Appl. Phys. **53**(30), 305004 (2020).
46. V. S. Yadav, S. K. Ghosh, S. Bhattacharyya, and S. Das, "Graphene-based metasurface for a tunable broadband terahertz cross-polarization converter over a wide angle of incidence," Appl. Opt. **57**(29), 8720–8726 (2018).
47. A. Li, S. Singh, and D. Sievenpiper, "Metasurfaces and their applications," Nanophotonics **7**(6), 989–1011 (2018).
48. J. Zhu, W. Tang, C. Wang, C. Huang, and Y. Shi, "Dual-polarized bandpass frequency-selective surface with quasi-elliptic response based on square coaxial waveguide," IEEE Trans. Antennas Propag. **66**(3), 1331–1339 (2018).
49. J. Luo, Y. Yang, Z. Yao, W. Lu, B. Hou, Z. H. Hang, C. T. Chan, and Y. Lai, "Ultratransparent media and transformation optics with shifted spatial dispersions," Phys. Rev. Lett. **117**(22), 223901 (2016).
50. Z. Yao, J. Luo, and Y. Lai, "Photonic crystals with broadband, wide-angle, and polarization-insensitive transparency," Opt. Lett. **41**(21), 5106–5109 (2016).
51. K. Im, J.-H. Kang, and Q.-H. Park, "Universal impedance matching and the perfect transmission of white light," Nat. Photonics **12**(3), 143–149 (2018).
52. M. Kerker, D.-S. Wang, and C. Giles, "Electromagnetic scattering by magnetic spheres," J. Opt. Soc. Am. **73**(6), 765–767 (1983).
53. R. Paniagua-Domínguez, Y. F. Yu, A. E. Miroshnichenko, L. A. Krivitsky, Y. H. Fu, V. Valuckas, L. Gonzaga, Y. T. Toh, A. Y. S. Kay, B. Luk'yanchuk, and A. I. Kuznetsov, "Generalized brewster effect in dielectric metasurfaces," Nat. Commun. **7**(1), 1–9 (2016).
54. D. R. Abujetas, J. A. Sanchez-Gil, and J. J. Sáenz, "Generalized brewster effect in high-refractive-index nanorod-based metasurfaces," Opt. Express **26**(24), 31523–31541 (2018).
55. W. Liu and Y. S. Kivshar, "Generalized kerker effects in nanophotonics and meta-optics," Opt. Express **26**(10), 13085–13105 (2018).
56. Z. Zhang, Z. Che, X. Liang, J. Chu, J. Zeng, H. Huang, F. Guan, L. Shi, X. Liu, and J. Zi, "Realizing generalized brewster effect by generalized kerker effect," Phys. Rev. Appl. **16**(5), 054017 (2021).
57. J. Olmos-Trigo, C. Sanz-Fernández, D. R. Abujetas, J. Lasa-Alonso, N. de Sousa, A. García-Etxarri, J. A. Sánchez-Gil, G. Molina-Terriza, and J. J. Sáenz, "Kerker conditions upon lossless, absorption, and optical gain regimes," Phys. Rev. Lett. **125**(7), 073205 (2020).